Applied Surface Science 270 (2013) 418–427

Contents lists available at SciVerse ScienceDirect

Applied Surface Science

journal homepage: www.elsevier.com/locate/apsusc

Novel high damage-tolerant, wear resistant $MoSi_2$-based nanocomposite coatings

Jiang Xu[a,*], Zhengyang Li[b,*], Zong-Han Xie[c], Paul Munroe[d], Xiao Lin Lu[a], Xiu Feng Lan[a]

[a] Department of Material Science and Engineering, Nanjing University of Aeronautics and Astronautics, 29 Yudao Street, Nanjing 210016, PR China
[b] Institute of Mechanics, Chinese Academy of Sciences, Beijing, 100190, PR China
[c] School of Mechanical Engineering, University of Adelaide, SA 5005, Australia
[d] School of Materials Science and Engineering, University of New South Wales, NSW 2052, Australia

ARTICLE INFO

Article history:
Received 26 October 2012
Received in revised form 5 January 2013
Accepted 7 January 2013
Available online 11 January 2013

Keywords:
Nanocomposites
Mechanical properties
Wear
Coatings

ABSTRACT

In this study, novel $MoSi_2$-based nanocomposite coatings were deposited on Ti-6Al-4V substrates by a two-step process involving firstly, deposition of $MoSi_2$-based coatings, using a double cathode glow discharge process and, secondly, plasma nitridation of the as-deposited coatings. The aim of this latter step is to introduce nitrogen into the coating and promote the formation of amorphous silicon nitride. The resulting coatings were characterized by X-ray diffraction (XRD), X-ray photoelectron spectroscope (XPS), transmission electron microscopy (TEM) and scanning electron microscopy (SEM). It was found that the nanocomposite coatings were composed of nanocrystallite Mo_5Si_3 and $MoSi_2$ grains embedded in an amorphous Si_3N_4 matrix. The mechanical properties and damage resistance of the coatings were evaluated by both Vickers indentation and nanoindentation techniques. Dry sliding wear tests were performed using a ball-on-disc type tribometer, in which the coated samples were tested against a ZrO_2 ceramic ball at normal loads of 2.8 and 4.3 N under ambient conditions. Compared with the monolithic $MoSi_2$ nanocrystalline coating, the specific wear rates of the nanocomposite coatings decreased by an order of magnitude. The specific wear rate was further improved by about 20% through the addition of Al, which was attributed to an optimum combination of mechanical properties.

1. Introduction

Among refractory metal silicides, molybdenum disilicide ($MoSi_2$) has attracted much attention as a promising coating material suitable for extremely harsh working conditions. This is due to its unique combination of high melting point (2030 °C) and excellent high-temperature oxidation resistance [1,2]. Unfortunately, its low toughness (2∼3 MPa $m^{1/2}$) poses a serious obstacle to its commercial application [3,4]. For example, $MoSi_2$ is expected to be an attractive wear-resistant material due to its high hardness and elastic modulus [5–7]. However, the wear resistance of hard coatings is known to rely on their mechanical properties, in particular fracture toughness [8]. Therefore, high damage tolerance is vital to effective wear performance.

Various attempts have been made to tackle the low toughness of $MoSi_2$ [9,10]. Since $MoSi_2$ is thermodynamically stable with a variety of ceramic reinforcements, $MoSi_2$-based composites have been made through the addition of SiC [11], Si_3N_4 [12] and Al_2O_3 [13] to improve its toughness. Among them, $MoSi_2$–Si_3N_4 composites are especially attractive, because they possess not only good toughness, but also high temperature creep strength as compared to monolithic $MoSi_2$. This has been attributed to the good chemical compatibility between Si_3N_4 and $MoSi_2$ [14,15]. On the other hand, metallic bonding exists in $MoSi_2$, making it possible to improve toughness through an alloying approach [16]. So far, aluminum has been the most common alloying element addition to $MoSi_2$, where it has been shown that the substitution of Al for Si enhances the toughness of $MoSi_2$, as well as increasing its oxidation resistance [17,18].

However, the extent to which the toughness of $MoSi_2$ can be achieved through either alloying or composite engineering is still limited. Recent studies have shown that the integration of several different toughening strategies may be a viable route to significantly improve the damage resistance of $MoSi_2$. For instance, Mitra et al. [19] reported that a $MoSi_2$–Al_2O_3 composite containing 9 at.% Al exhibits a considerable increase in the fracture toughness (i.e., ∼49%) as compared to monolithic $MoSi_2$. However, there is a lack of understanding about how different toughening strategies in $MoSi_2$ may affect its wear behavior. In the present study, novel $MoSi_2$-based nanocomposite coatings are prepared in situ on Ti-6Al-4V substrates first by the sputter-deposition of a $MoSi_2$ coating, containing about 5 at.% Al, followed by plasma nitriding. The aim of the plasma nitridation step is to promote the formation of amorphous silicon nitride as an interfacial phase between the molybdenum silicide grains. The combined effects of both Al alloying and the

* Corresponding authors.
E-mail addresses: xujiang73@nuaa.edu.cn (J. Xu), zhengyang.li@gmail.com (Z. Li).

0169-4332/$ – see front matter © 2013 Elsevier B.V. All rights reserved.
http://dx.doi.org/10.1016/j.apsusc.2013.01.041

formation of a nanocomposite structure on mechanical properties and wear resistance of the resultant coatings were examined and clarified.

2. Experimental method

The substrate material was Ti-6Al-4V in the form of disks with a diameter of 40 mm and a thickness of 3 mm. The nominal composition in wt.% was: Al, 6.04%; V, 4.03%; Fe, 0.3%; C, 0.1%; H, 0.015%; N, 0.05%; O, 0.15% and the balance, Ti. Before deposition, the Ti-6Al-4V substrates were polished using silicon carbide abrasive paper of 2400 grit and then ultrasonically cleaned in pure alcohol. Two kinds of nanocrystalline $MoSi_2$ coatings containing either 0 at.% or 5 at.% Al were pre-deposited on the mirror-polished substrate by a double cathode glow discharge apparatus using two targets with different stoichiometric ratios ($Mo_{25}Si_{75}$ and $Mo_{25}Si_{65}Al_{10}$), respectively. The reasons for such a difference in the composition of the targets and the as-deposited coatings are that the composition of the as-deposited coatings is related to not only the composition of targets materials, but also the sputtering yields of the various elements in the target materials. Furthermore, the diffusion of different alloying elements at the interface between the as-deposited coatings and substrate also affects the final composition of the coatings. In this deposition process, glow-discharge sputtering conditions were: base pressure, 4×10^{-4} Pa; target electrode bias voltage, −900 V; substrate bias voltage, −350 V; substrate temperature, ∼800 °C; working pressure, 35 Pa; target-substrate distance, 10 mm and treatment time 3 h. Subsequently, plasma nitriding of the two $MoSi_2$ coatings was performed in a mixture of Ar and N_2 atmosphere with a Ar:N_2 molar ratios of 20:1 at a working pressure of 35 Pa. The plasma nitriding process was run at 600 °C by adjusting direct current bias voltage (−600 V), and the nitriding time was set at 2 h. For the sake of brevity, the untreated binary $MoSi_2$ coating and the two $MoSi_2$ coatings containing 0 at.% and 5 at.% Al is subsequently subjected to plasma nitriding, are referred to as MN, AN0 and AN5, respectively.

The phase compositions of the as-deposited coatings were studied by X-ray diffractometry (XRD, D8ADVANCE with Cu Kα radiation) operated at 35 kV and 40 mA. X-ray data were collected using a 0.1° step scan with a count time of 1 s. The microstructures of the as-deposited coatings were examined using scanning electron microscopy (SEM, Sirion 400NC, FEI Company) incorporating an X-ray energy dispersive spectroscopy (EDS, EDAX Inc.) analyzer attachment and field emission transmission electron microscopy (FEG-TEM, Philips CM200, Eindhoven, Netherlands). The etching of the as-deposited coatings was accomplished with the use of Kroll's reagent (10 ml HNO_3, 4 ml HF and 86 ml distilled water) for 20–30 s. Thin-foil specimens for plan-view TEM samples were prepared by cutting, grinding, dimpling and a final single-jet electropolishing from the untreated side of the substrate at low temperature. X-ray photoelectron spectroscope (XPS) measurements were carried out by Kratos AXIS Ultra ESCA System using Al Kα (1486.71 eV, pass energy of 20 eV).

Nanoindentation tests were conducted on all the as-deposited coatings using a nanoindentation tester (NHT) equipped with a Berkovich diamond tip. This system, developed by CSEM Instruments, comprises two distinct components: a measuring head for performing nanoindentation and an optical microscope for selecting a specific sample site prior to indentation, and for checking the location of the imprint after indentation. The system has load and displacement resolutions of 10 μN and 1 nm, respectively. Fused silica was used as a standard sample for the initial tip calibration. The indentation was performed by driving the indenter at a constant loading rate of 40 mN/min into the material surface with the maximum applied load of 20 mN. Hardness and the elastic modulus were evaluated using the Oliver–Pharr method [20] based on the load-displacement data obtained during the indentation tests. Each hardness and elastic modulus data were derived from the load-displacement curves of at least five indentations to ensure repeatability of the experimental data.

The friction and wear tests were conducted using a HT-500 ball-on-disc type tribometer under dry conditions at room temperature in air with a relative humidity of 40–45%. In the present work, the balls, each 3 mm in diameter, were made of ZrO_2 with a hardness of 1300HV and the lower disc samples (10 mm × 10 mm × 3 mm) were machined from both the uncoated substrate and the coated alloys. During the wear test, the ceramic ball was slid on the specimen surface describing a circle with a diameter of 6 mm at a sliding velocity of 0.176 m/s under the applied normal loads of 2.8 and 4.3 N, respectively. The friction coefficient was continuously recorded using a Dell PC connected to the ball-on-disc test ring. The duration time of each test was 60 min, which corresponded to a sliding distance of 633.6 m. The profiles of the worn surfaces were measured using a MicroXAM^{TM} non-contact optical profilometer (ADE Phase-Shift, USA) and the worn volume loss was evaluated by calculating the cross-sectional areas of worn tracks developed on the surface of the samples. The morphology and chemical compositions of worn surfaces were analyzed by SEM (SEM, Quanta200, FEI Company)-EDX.

3. Results

3.1. Microstructures and phase analysis

X-ray diffraction patterns were collected from the MN, AN0 and AN5 coatings. As shown in Fig. 1(a), only monolithic C40-structured $MoSi_2$ phase, with a strong (1 1 1) preferred orientation, was identified in the MN coating. However, after plasma nitriding, both the C40-structured $MoSi_2$ phase and the $D8_m$-structured Mo_5Si_3 phase were detected in the AN0 and AN5 coatings. Note that Al atoms have a larger atomic radius than Si. With the addition of Al, the diffraction peaks for both the $MoSi_2$ and Mo_5Si_3 phases in the AN5 coating were shifted toward lower 2θ angles in comparison with the AN0 coating, indicating that the lattice parameter increases as Al substitutes for Si in both compounds. Further, closer examination of the XRD patterns of the plasma nitrided coatings suggested the presence of a diffuse peak, starred in the spectra, over a 2θ range of 25–29° roughly centered around 27°. Such a diffuse peak is indicative of the presence of amorphous Si_3N_4 phase. Consequently, the following reaction is expected to occur during the plasma nitriding process:

$$15MoSi_2(s) + 14N_2(g) \rightarrow 3Mo_5Si_3(s) + 7Si_3N_4(s) \quad (1)$$

This result is consistent with observations of Guo et al. [21] who reported that $MoSi_2$ when reacted in a N_2 atmosphere during sintering, formed Mo_5Si_3. To obtain further information on the chemical bonding state of the Si atoms in the nitrided layer, XPS analysis was performed on the MN and AN coatings. The Si 2p spectrum obtained from MN coating (Fig. 1(b)) shows one component with a binding energy of 99.1 eV, corresponding to $MoSi_2$. Deconvolution of the Si 2p spectrum collected from AN coatings reveals the presence of three peaks centered at 101.75, 99.55 and 99.1 eV, respectively (Fig. 1(c)). The peak located at the highest binding energy (101.75 eV) corresponds to stoichiometric Si_3N_4 [22], whereas the peak at the lowest binding energy (99.1 eV) can be attributed to the presence of $MoSi_2$. Although the Si 2p binding energy for Mo_5Si_3 is not known, one can assume, supported by the XRD data, that the peak resolved at a binding energy of 99.55 eV originates from Mo_5Si_3. The calculation of relative concentrations, using the areas of the peaks, indicates that the relative ratio of Si_3N_4 to Mo_5Si_3 approximates to the values predicted by reaction

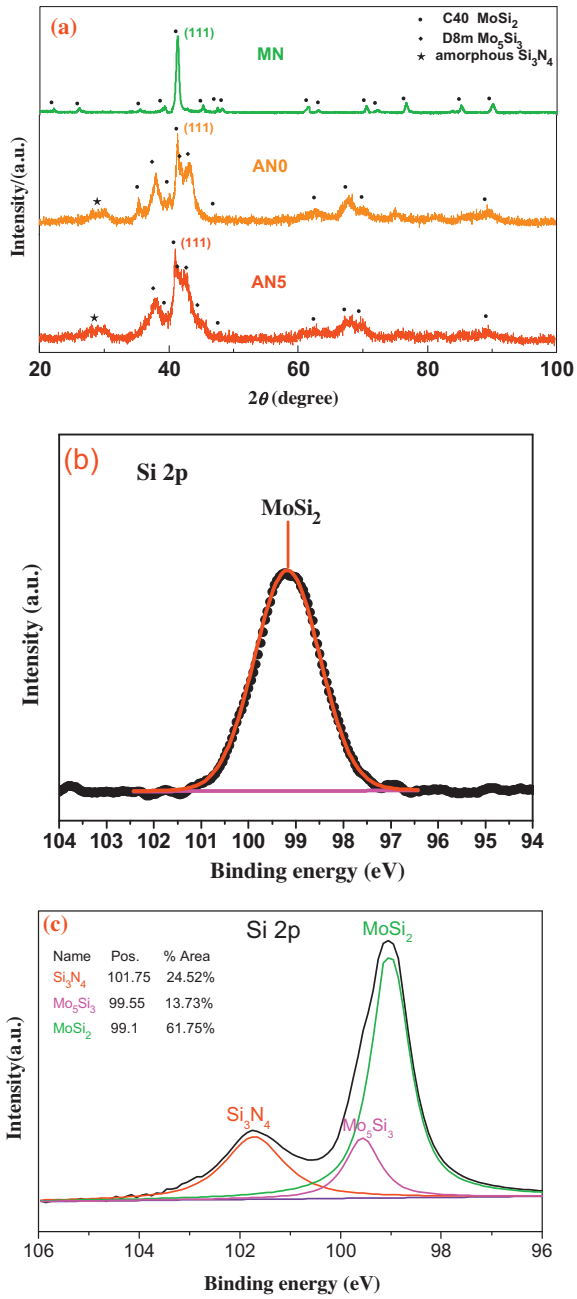

Fig. 1. (a) XRD patterns of the three coatings. The high-resolution XPS spectra for Si 2p collected from MN coating (b) and AN0 coating (c).

(1), and, thus, in our case partial nitridation of $MoSi_2$ has occurred, leading to the formation of composite coatings consisting of $MoSi_2$, Mo_5Si_3 and Si_3N_4 phases. Fig. 2(a)–(c) shows typical cross-section SEM images and the corresponding EDS line-scans of the MN, AN0 and AN5 coatings, respectively. Notably, these coatings are free of cracking and appear compact and well adhered to the Ti-6Al-4V substrate. The as-deposited MN coating (Fig. 2(a)) consists of an outer layer of monolithic C40-$MoSi_2$ with a thickness of ~15 μm and the inner Mo diffusion layer. The Mo diffusion layer is generated by Mo atoms diffusing from the outer layer into the substrate, and may be subdivided into a β-Ti layer with a higher Mo content (>10 wt.%) and an α″/α′-Ti layer with a lower Mo content (<10 wt.%), as described elsewhere [23]. For the AN0 and AN5 coatings (Fig. 2(b) and (c)), a 5 μm thick outer layer has been partly nitrided and its microstructure is composed of $MoSi_2$ (or $Mo(Si,Al)_2$), Mo_5Si_3(or $Mo_5(Si,Al)_3$) and Si_3N_4 phases. Fig. 3(a) and (b) show typical plan-view TEM bright-/dark-field images obtained from the MN coating and the corresponding selected area electron diffraction (SAED) pattern of the outer $MoSi_2$ layer. Clearly, the outer layer consists of nearly rounded grains with an average grain size of 5 nm, and the strong diffracted intensity in the $MoSi_2$ (1 1 1) reflection provides further evidence that the MN coating exhibits a strong (1 1 1) texture. In comparison, the AN0 coating consists of grains of different sizes (Fig. 3(c)). The associated diffraction pattern exhibits one intense ring, plus two fainter rings. These three rings were indexed to be consistent with the (1 1 1), (1 1 4) and (3 1 1) lattice planes of $MoSi_2$, superimposed with an intense background on the inside of (1 1 1) ring, which further confirms that the nanocomposite structure is characterized by a mixture of amorphous and crystalline phases. Fig. 3(d)–(f) shows high-resolution electron microscopy (HRTEM) images of the MN, AN0 and AN5 coatings, respectively. As shown in Fig. 3(d), the lattice fringes of 0.218 nm (marked with circles) correspond to d spacing of (1 1 1) plane of $MoSi_2$. On the contrary, the AN0 and AN5 coatings show a very similar microstructure feature, in which the rounded "coarse" Mo_5Si_3 grains and the rounded fine $MoSi_2$ grains are separated by amorphous Si_3N_4 layer with atomically sharp crystalline/amorphous interfaces.

3.2. Nanoindentation testing

Fig. 4(a) shows the representative load–displacement (P–h) curves for the coatings under a maximum load of 20 mN. Note that the maximum indentation depth is smaller than 10% of the coatings thickness, indicating that the contribution to measured mechanical properties from the substrate might be negligible. The penetration depths and residual depth of AN0 and AN5 coating are shallower than that of the MN coating, suggesting a significant improvement in hardness for the nanocomposite coatings. Moreover, the unloading parts of both nitrided coatings are very similar, suggesting a close resemblance in their elastic properties. The hardness (open symbol) and elastic modulus values (solid symbols) calculated from the load–displacement curves are plotted in Fig. 4(b). As shown in Fig. 4(b), the hardness of the as-deposited MN coating was determined to 23 GPa, which is substantially larger than the theoretical hardness of C40 $MoSi_2$ (10.15 GPa)[24], and also larger than that of $C11_b$ $MoSi_2$ with an average grain size of 38 nm (16.3 GPa) [25]. In addition, the elastic modulus of the as-deposited MN coating is slightly higher than the theoretical value of 341 GPa for C40 $MoSi_2$ [24]. Generally, the elastic modulus reflects, to some extent, the density of the material, and several studies have reported that a reduction in elastic modulus correlates well with the existence of the micro-defects in nanostructured materials [26,27]. Therefore, this suggests that the coatings synthesized in this study exhibit highly dense structures. Compared with the MN coating, the hardness increases by 43% for AN0 and 30% for AN5 coatings, whereas the elastic modulus is reduced by 15% for AN0 and 27% for AN5. It is known that the plastic deformation of materials is strongly dependent on the formation and movement of dislocations. However, as grain sizes are reduced to the nanometer scale, dislocation-mediated deformation is inhibited due to the lack of dislocation activity. Consequently, the nature of grain boundaries is critical to the deformation of nanostructured materials, and this process requires more energy than deformation by dislocation movement. If dislocations should have formed in the crystallites under a highly applied stress, they are not able to move freely through the amorphous matrix, and hence a higher hardness can be achieved for such nanocomposite coating structure [31]. Moreover, first-principle simulations indicate that the presence of a thin amorphous boundary layer can effect strong bonding between the nanocrystalline grains and greatly enhance coating hardness [32]. Vepřek et al. [28–30] prepared a series of

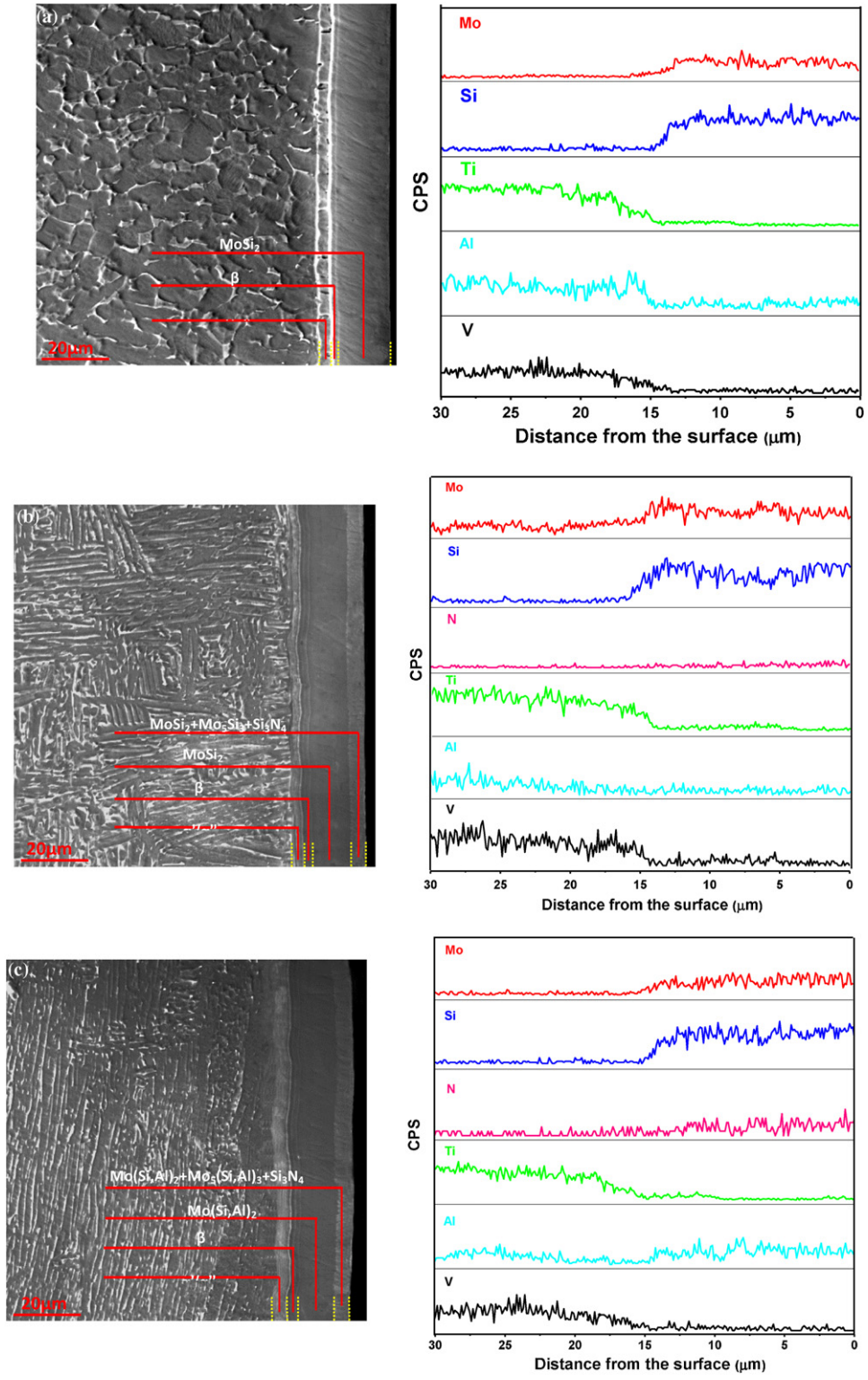

Fig. 2. Cross-section SEM images of the three coatings and the concentration profiles of the elements from the EDS line scan across the entire thickness of the three coatings:(a) MN, (b) AN0 and (c) AN5.

nanocomposite thin films, in which transition-metal nitrides nanocrystals having a size smaller than 10 nm. For example TiN, W_2N and VN, were embedded in either an amorphous Si_3N_4 or BN grain boundary phase. The resulting composite coatings showed a substantial increase in hardness as compared with transition-metal nitrides alone. Fig. 4(c) shows the H^3/E^2 and $1/E^2H$ ratios derived from the measured values of E and H for the three coatings. The ratio H^3/E^2 for AN0 and AN5 is about 3.8 times higher than that of MN coating, while the ratio $1/E^2H$ of AN5 coating is about 1.5 times greater than that of both MN and AN0. According to classic contact mechanics, the critical load for yielding of solids, Py, is proportional to H^3/E^2, indicating that H^3/E^2 is a good indicator of a

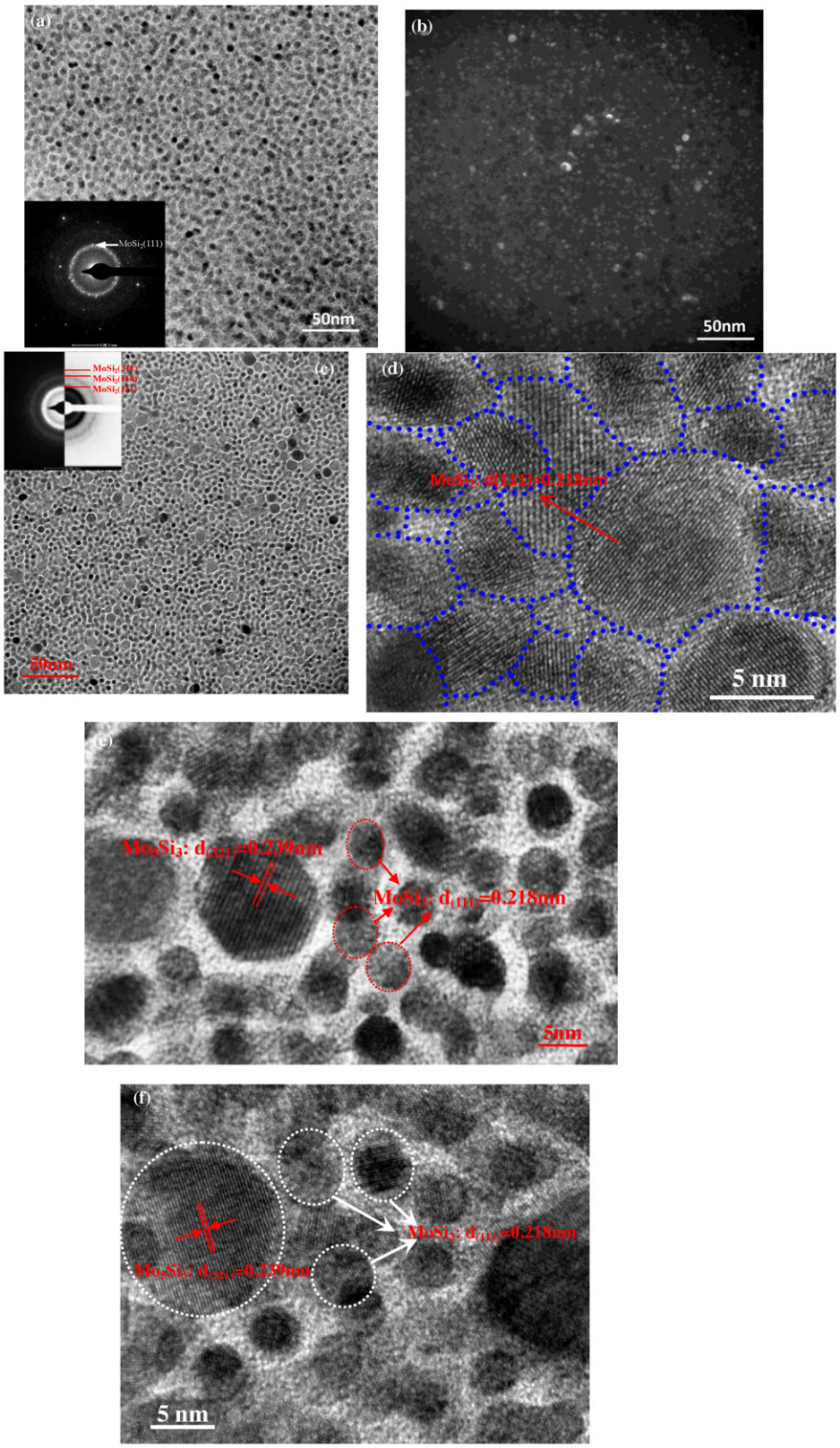

Fig. 3. (a) Bright-field and (b) dark-field TEM images of outer $MoSi_2$ layer obtained from the MN coating. The inset in Fig. 3(a) is SAD pattern of $MoSi_2$ phase. (c) A plan-view TEM bright-field image of nitrided layer obtained from AN0 coating with corresponding selected area electron diffraction (SAED) pattern. High-resolution electron microscopy (HRTEM) images of outer layer obtained from MN (d), AN0 (e) and AN5 (f) coatings.

coating's resistance to abrasion damage caused by localized plastic deformation against a blunt rigid contact [33,34]. Additionally, the threshold load for crack initiation varies linearly with $1/E^2H$, which can thus be used as an index to forecast the tolerance of a coating to abrasion damage resulting from microcracking [35]. Based up this analysis, the damage resistance of the $MoSi_2$-based composite coatings may be enhanced by both plasma nitriding and Al alloying.

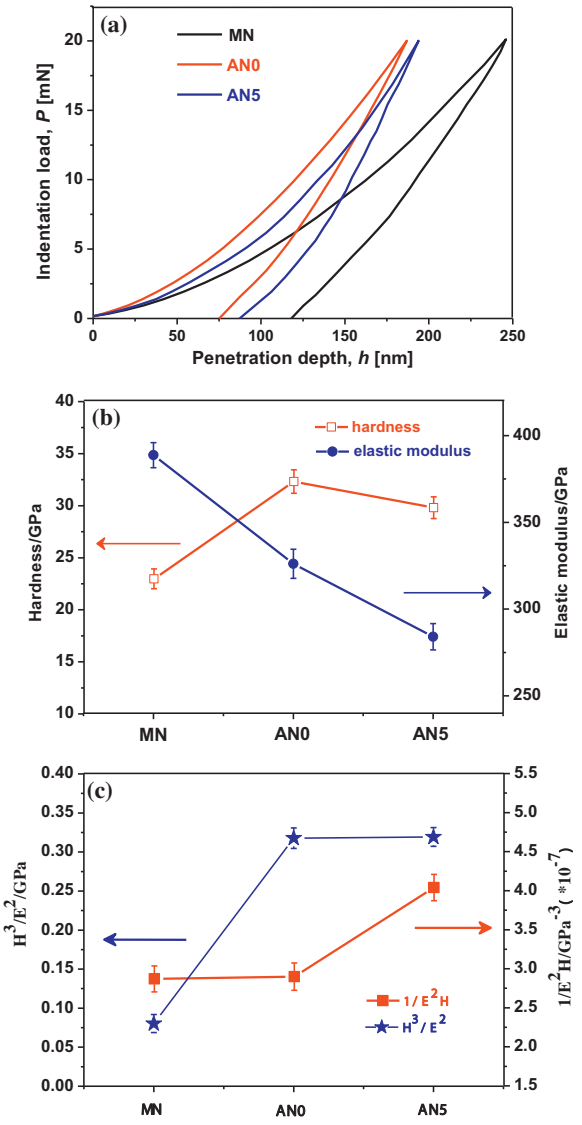

Fig. 4. (a) Load–displacement curves of the three coatings; (b) the hardness and elastic modulus of the three coatings;(c) the H^3/E^2 and $1/E^2H$ ratios derived from the measured values of E and H for the three coatings.

3.3. Indentation damage tests

The contact-damage resistance of the coatings was evaluated using a Vickers hardness tester. Fig. 5(a–c) shows representative optical micrographs of Vickers indentation impressions generated on the surface of the three coatings. No crack formation or propagation can be detected at the corners of the indents, even at an applied load of 1000 g, for all three coatings. In contrast, cracks emanating from the corners of indent impressions have been observed at applied loads less than or equal to 1000 g, for coarse-grained monolithic $MoSi_2$, Mo_5Si_3 and coarse-grained $MoSi_2$–SiC composite materials [36–38]. Patel et al. also indented a $MoSi_2$–SiC nanocomposite with an average grain size of 60 nm under a load of 500 g, and found radial cracks extending out from the corners of the indentations [39]. In comparison to these materials, the three coatings studied here exhibit a higher damage tolerance, suggesting that the more energy is required to initiate the cracks.

For thin films or coatings, the employment of a larger indentation load for damage assessment is undesirable due to the coating thickness limitations. For this reason, a qualitative method of damage analysis, in which cracks are induced by the interactions of stress fields caused by neighboring indents, was used to further evaluate the damage tolerance of the three coatings. When the distance between any two neighboring indentations (D) are set as about twice the Vickers indentations diagonal length (L), indentation-induced cracks appear in the MN coating under a load of 300 g (Fig. 5d), whereas no cracks are visible on the surface of the as-deposited AN0 coating at the same load (Fig. 5e) until the indentation load reaches 1000 g (not shown here). This implies that the $MoSi_2$-based nanocomposite coating has a higher damage tolerance. Surprisingly, no radial cracks were detectable for AN5 even under an indentation load of 1000 g, revealing that the addition of Al enhances the damage tolerance of $MoSi_2$-based nanocomposite coatings with little reduction of hardness.

3.4. Friction and wear experiments

Fig. 6(a) and (b) show the variations of friction coefficient as a function of time for the three coatings and the uncoated substrate sliding against ZrO_2 ceramic balls under two different loads. It is noted that the friction coefficients of all tested samples increase rapidly during the initial run-in stage, followed by a stage where the coefficients of friction fluctuate within a narrow range around the average value. During this stage, the average friction coefficient for MN coating is higher than that of the uncoated substrate at a normal load of 2.8 N, while an opposite tendency is observed at the higher normal load of 4.3 N. In comparison, the AN0 and AN5 coatings exhibits appreciably smaller fluctuations in friction response and lower average values of friction coefficient under each load applied. In addition, for the three coatings, their friction coefficients decrease with an increasing load, whereas the friction coefficient of the uncoated substrate increases with an increase in applied load. Lim and Ashby [40] indicated that the friction coefficient depended on the real contact area, the contact state and the lubricating role of debris. During the dry sliding wear process, it is expected that friction-induced temperature increases with normal load and the material softens leading to an increase in real contact area. This would result in an increase of friction coefficient of the uncoated substrate at higher normal loads. For the three coatings, however, a decrease of friction coefficient with load is observed. This may result from the generation of a lubricating surface layer through tribo-chemical reactions when the normal load increases, which will be discussed in detail in the next section.

In Fig. 6(c), the variation of specific wear rates with the applied normal load for the coatings is plotted against that for the uncoated substrate for a fixed sliding time of 60 min. The specific wear rates increase with the applied normal loads for all of tested samples, but the rise of specific wear rates of the nitrided coatings were less sensitive to the applied loads. More importantly, the nitriding treatment dramatically reduced the wear rate of the coatings under each load. Compared with the MN coating, the specific wear rates of the AN0 coating decrease by one order of magnitude, and further decrease by about 20% for the AN5 coating. Fig. 7 shows SEM micrographs of worn surface of the three coatings sliding against ZrO_2 ceramic balls under normal loads of 4.3 N. Many craters are visible on the worn surface of the MN coating (Fig. 7(a)), and at the higher magnification, microcracks and delaminations at the bottom of these craters can be readily seen (Fig. 7(b)). These are caused by the friction-induced tensile stresses at the trailing edge of the indenter. Hence, the wear damage of the MN coating is governed by fracture processes, which generate large wear debris and make contact conditions unstable. This may explain relatively the large fluctuations in the observed friction coefficient curves. Distinct from the MN coating, the wear tracks of the AN0 and AN5 coatings appear to be very smooth, showing no sign of any peeling off or spallation, as shown in Fig. 7(c) and (d). Moreover, EDS spectra of the wear tracks suggest the presence of oxides, indicating that

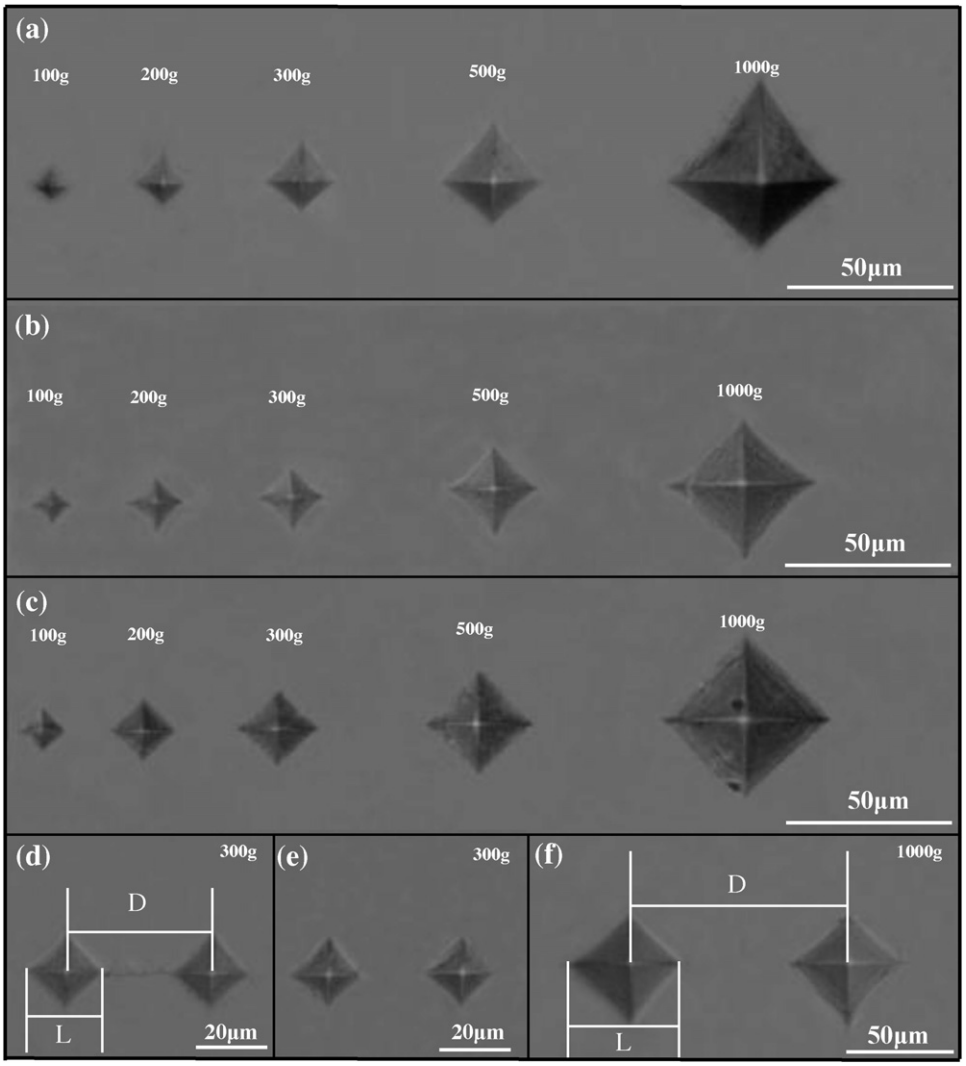

Fig. 5. Optical micrographs of Vickers indentations in (a) MN, (b) AN0 and (c) AN5 coatings at applied loads ranging from 100 g to 1000 g. Overlap of Vickers indentation: (d) MN coating with a load of 300 g; (e) AN0 coating with a load of 300 g; (f) AN5 coating with a load of 1000 g.

tribochemical reactions may take place during the wear process. To further elucidate the nature of these oxides, XPS analysis was performed on the AN0 coating. Fig. 8 shows high-resolution XPS spectra for the Mo 3d, Si 2p and O 1s peaks collected from the worn surface of the AN0 coating. In Fig. 8(a), the measured spectrum of the Mo 3d consists of doublet peaks Mo $3d_{5/2}$ and Mo $3d_{3/2}$ at 233 and 236.1 eV which originates from the MoO_3 phase. A single Si 2p peak (Fig. 8(b)) was detected at a binding energy of 103 eV, which corresponds to the presence of SiO_2. The spectrum of O 1s (Fig. 8(c)) exhibits single broad peak, which can be resolved into two overlapping peaks located at approximately 532.3 and 530.93 eV. They correspond to the presence of SiO_2 (79.67%) and MoO_3 (20.33%).

4. Discussion

The microstructural characterization of the AN0 and AN5 coatings reveal that the partial nitridation of $MoSi_2$ gives rise to a unique nanocomposite structure composed of nanocrystalline $MoSi_2$ and Mo_5Si_3 phases bonded together by an interfacial amorphous Si_3N_4 layer. The thickness of this layer is known to be vital to control the mechanical properties, in particular damage resistance of this type of nanocomposite. Vepřek et al. [41] reported that the presence of a 0.3–0.5 nm thick amorphous Si_3N_4 layer significantly enhances the hardness of nc-Me_nN/a-Si_3N_4 films by a coherence strain-induced effect, due to the fact that the average thickness of the silicon nitride between the nanocrystallites TiN is evidently too small to relax the coherence strain at the interfaces and to facilitate mutual sliding of the nanograins. The theoretical concept for the design of this class of superhard coatings is based on the simple idea that a high cohesive energy and high elastic modulus determine the hardness. Unfortunately, the fairly linear dependence of the hardness on the elastic modulus provides direct evidence for the lack of the ductility in these superhard nanocomposite films. However, in this case, the following aspects are responsible for the increase in toughness of the AN0 and AN5 coatings in contrast to that of the MN coaing: owing to the combination of the fourfold coordinated silicon with the threefold coordinated nitrogen, Si_3N_4 has a large structural flexibility to accommodate the strain at the incommensurable a nanocrystalline metal silicide/amorphous phase interface [42]. Because the average width of the amorphous Si_3N_4 layer is about 2.3 nm for the AN0 and AN5 coatings, the "thick" amorphous Si_3N_4 layer comprising three dimensional network, can prevent interaction between atomic planes in the adjacent grains and allow plastic flow to occur along the grain boundaries through individual atomic displacements to release the accumulated strain, rather than inhibiting mobility of grains boundary as in the case where the thickness of amorphous grain boundary less than 1 nm[43]. Interestingly, many natural composites consisting

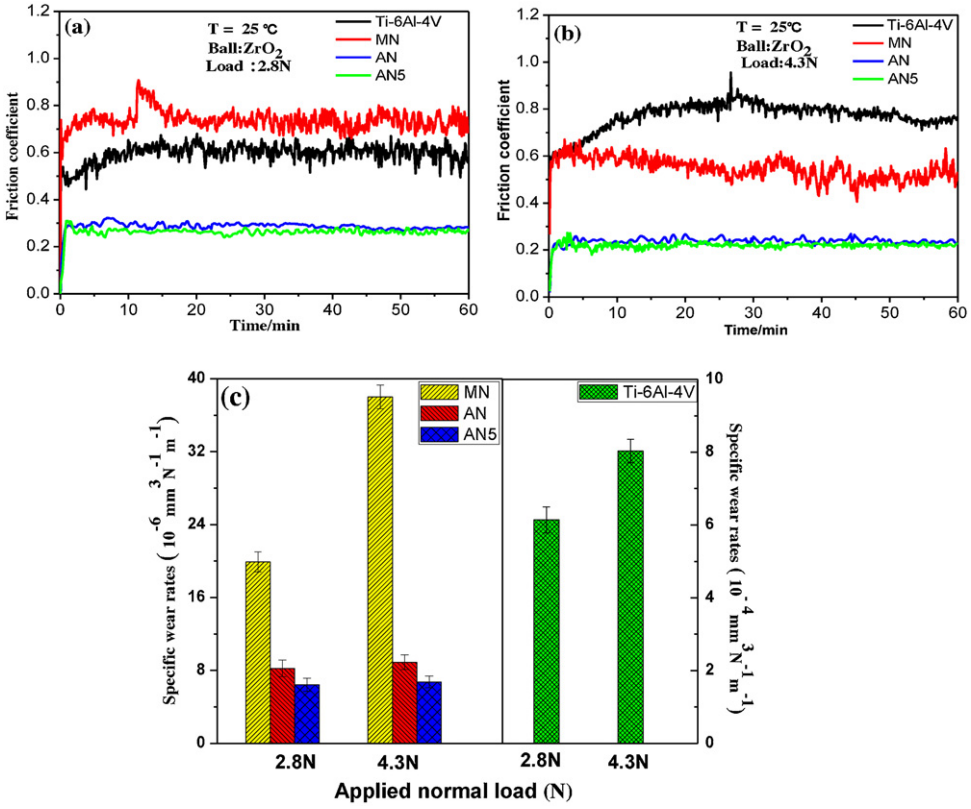

Fig. 6. Coefficient of friction vs. sliding times for the three coatings and the uncoated substrate sliding against ZrO_2 ceramic balls under two different loads: (a) 2.8 N and (b) 4.3 N. (c) The variation of specific wear rates versus applied normal load for the three coatings and the uncoated Ti-6Al-4V substrate.

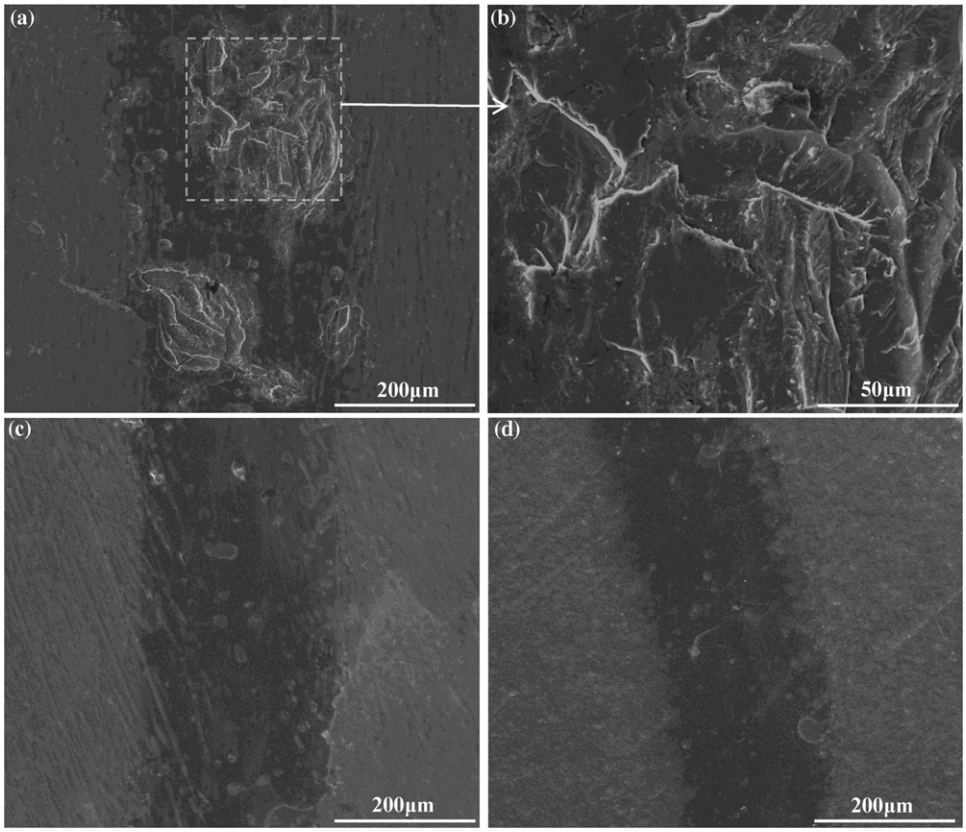

Fig. 7. SEM micrographs of worn surface of the three coatings sliding against ZrO_2 ceramic ball under the normal loads of 4.3 N: (a) MN coating; (b) higher magnifications of a selected area in (a); (c) AN0 coating and (d) AN5coating.

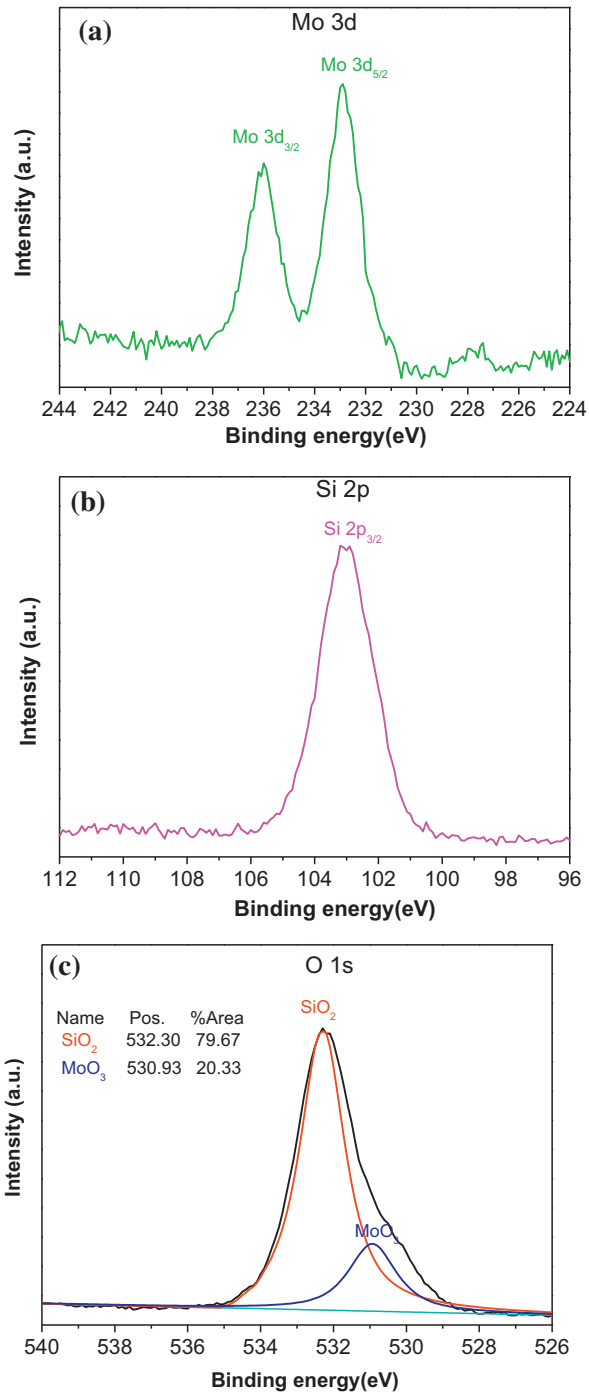

Fig. 8. High-resolution XPS spectra obtained from the worn surface on the AN0 coating: (a) Mo 3d, (b) Si 2p and (c) O 1s.

of biominerals of high stiffness and strength held together by very thin, soft protein layers exhibit a unique combination of high hardness, stiffness and fracture toughness. One intriguing example is nacre, which is composed of at least 95 wt.% of calcium carbonate ($CaCO_3$) in the form of hexagonal aragonite platelets separated by thin biopolymer layers consisting of proteins and/or polysaccharides. Such nanocomposite microstructure results in enhanced crack deflection along the interface, which promotes the effective redistribution of contact-induced stresses, yielding an ~8-fold increase of fracture toughness over monolithic $CaCO_3$ [44]. A recent theoretical study reveals that one significant contribution to nacre's extraordinary mechanical properties is its spatial variation of the elastic modulus associated with the alternating inorganic/organic structure, since thin, soft layers arrest cracks, strongly reducing the crack driving force [45]. Therefore, it would be expected that as the variation in elastic modulus become greater, crack propagation is more effectively suppressed [46,47]. Similarly, for the two $MoSi_2$-based nanocomposite coatings where the multiphase structures with various elastic moduli ($MoSi_2$ ($E_{MOSi_2} = 388$ GPa), Mo_5Si_3 ($E_{MO_5Si_3} = 323.0$ GPa) [48] and a-Si_3N_4 ($E_{Si_3N_4} = 232.0$ GPa) [49]) are combined at various length scales, soft a-Si_3N_4 layer helps reduce the crack driving force and increase crack growth resistance. With a further reduction in elastic modulus through Al alloying, it is reasonable to conjecture that the beneficial effects of Al alloying on toughness may be linked to the increased disparity in elastic modulus amongst the three phases. Zhang et al. [50] also found that doping of Al, can significantly reduce the hardness of a-C films, which is propitious to an improvement in toughness of a nc-TiC/a-C(Al) nanocomposite film. Moreover, when these coatings are subjected to excessive stress, the rounded $MoSi_2$ and Mo_5Si_3 nanosized grains with high angle grain boundaries can be expected to contribute to energy dissipation via grain boundary sliding assisted by grain boundary diffusion or rotation, analogous to the aragonite particles in natural nacre [51].

Based on the observations of the friction and wear behaviors and worn surfaces features, the wear process of the three as-deposited coatings is influenced primarily by their mechanical properties and the relevant tribochemical reactions which occur during wear testing. Generally, the wear rate of brittle materials is proportional to $H^{-1/2}K_{IC}{}^{-3/4}$, indicating that the wear resistance of brittle materials can be improved by increasing both hardness and fracture toughness [52]. In the present study, the unique features of the $MoSi_2$-based nanocomposite coatings yields both high hardness and toughness, leading to a lower wear rate, which is further improved by the incorporation of Al to obtain an optimum combination of mechanical properties. In addition, because of the high flash temperature induced by dry sliding wear, oxides, such as MoO_3 and SiO_2, were produced on the worn surface by tribochemical reactions, as confirmed by XPS and SEM-EDS investigations. These oxides, acting as solid lubricants, lower the tangential forces and prevent adhesive contact between the coatings and ZrO_2 balls, resulting in a significant reduction in friction coefficient and wear rates.

5. Conclusions

In summary, novel $MoSi_2$-based nanocomposite coatings consisting of nanocrystallites embedded in amorphous matrix have been prepared on Ti-6Al-4V substrates by plasma nitriding of pre-deposited $MoSi_2$ films, with varying Al contents, by a double cathode glow discharge apparatus. Compared with the monolithic $MoSi_2$ nanocrystalline coating, these newly developed nanocomposite coatings show a significant improvement in both hardness and toughness, and further improvement in toughness are achieved by the incorporation of Al with little reduction of hardness. The soft amorphous Si_3N_4 interfacial phase arrests cracks, strongly reducing the driving force for crack propagation. Compared with the monolithic $MoSi_2$ coating, the specific wear rates of the $MoSi_2$-based nanocomposite coatings decrease by one order of magnitude and wear resistance is further improved by the incorporation of Al to obtain an optimum combination of mechanical properties.

Acknowledgement

The authors acknowledge the financial support of the National Natural Science Foundation of China under grant No. 51175245.

References

[1] M. Patel, J. Subramanyuam, V.V. BhanuPrasad, Scripta Materialia 58 (2008) 211.
[2] J.J. Petrovic, A.K. Vasudevan, Material Science and Engineering, A 261 (1999) 1.
[3] J.J. Petrovic, Material Science and Engineering, A 192 (1995) 31.
[4] Y.T. Zhu, M. Stan, S.D. Conzone, D.P. Butt, Journal of American Ceramic Society 82 (1999) 2785.
[5] J.A. Hawk, D.E. Alman, Scripta Metallurgica et Materialia 32 (1995) 725.
[6] J.A. Hawk, D.E. Alman, J.J. Petrovic, Journal of American Ceramic Society 79 (1996) 1297.
[7] J.A. Hawk, D.E. Alman, J.J. Petrovic, Wear 203 (1997) 247.
[8] A.G. Evans, T.R. Wilshaw, Acta Metallurgica 24 (1976) 939.
[9] L. Sun, J.S. Pan, C.J. Lin, Materials Letters 57 (2003) 1239.
[10] P.Q. La, Q.J. Xue, W.M. Liu, Intermetallics 11 (2003) 541.
[11] L. Zheng, Y. Jin, P. Li, Composites Science and Technology 57 (1997) 463.
[12] S.J. Hong, V. Viswanathan, K. Rea, S. Patil, S. Deshpande, P. Georgieva, T. McKechnie, S. Seal, Materials Science and Engineering, A 404 (2005) 165.
[13] G.Y. Lin, V. Costil, Y. Jorand, G. Fantozzi, Ceramics International 25 (1999) 367.
[14] J.K. Yoon, G.H. Kim, J.H. Han, I.J. Shon, J.M. Doh, K.T. Hong, Surface and Coatings Technology 200 (2005) 2537.
[15] G. Wang, W. Jiang, G. Bai, D. Chen, Materials Letters 58 (2004) 308.
[16] J.J. Petrovic, Intermetallics 8 (2000) 1175.
[17] T. Dasgupta, A.M. Umarji, Intermetallics 15 (2007) 128.
[18] Y. Liu, G. Shao, P. Tsakiropoulos, Intermetallics 8 (2000) 953.
[19] R. Mitra, V.V. Rama Rao, A. Venugopal Rao, Intermetallics 7 (1999) 213.
[20] W.C. Oliver, G.M. Pharr, Journal of Materials Research 7 (1992) 1564.
[21] Z. Guo, G. Blugan, T. Graule, M. Reece, J. Kuebler, Journal of European Ceramic Society 27 (2007) 2153.
[22] A. Bendeddouche, R. Berjoan, E. Beche, T.M. Mejean, S. Schamn, V. Serin, G. Taillades, A. Pradel, R. Hillel, Journal of Applied Physics 81 (1997) 6147.
[23] J. Xu, Y. Wang, S.Y. Jiang, Nanoscale 2 (2010) 394.
[24] Y.J. Qiao, H.X. Zhang, C.Q. Hong, X.H. Zhang, Journal of Physics D: Applied Physics 42 (2009) 105413.
[25] T.J. Trentler, R.S. Iyer, S.M.L. Sastry, et al., Chemistry of Materials 13 (2001) 3962.
[26] P.G. Sanders, J.A. Eastman, J.R. Weertman, Acta Materialia 45 (1997) 4019.
[27] M.A. Meyers, A. Mishra, D.J. Benson, Progress in Materials Science 51 (2006) 427.
[28] S. Vepřek, S. Reiprich, S. Li, Applied Physics Letters 66 (1995) 2640.
[29] S. Vepřek, M. Haussmann, S. Reiprich, Journal of Vacuum Science and Technology A 14 (1996) 46.
[30] P. Karvankova, M.G.J. Veprek-Heijman, O. Zindulka, A. Bergmaier, S. Veprek, Surface and Coatings Technology 163 (2003) 149.
[31] B.S. Yau, J.L. Huang, D.F. Lii, S. Pavol, Surface and Coatings Technology 177 (2004) 209.
[32] R.F. Zhang, S. Veprek, Thin Solid Films 516 (2008) 2264.
[33] M. Dao, L. Lu, R.J. Asaro, J.T.M. De Hosson, E. Ma, Acta Materialia 55 (2007) 4041.
[34] A. Miserez, J.C. Weaver, P.J. Thurner, J. Aizenberg, Y. Dauphin, P. Fratzl, D.E. Morse, F.W. Zok, Advanced Functional Materials 18 (2008) 1241.
[35] J.C. Weaver, Q. Wang, A. Miserez, A. Tantuccio, R. Stromberg, K.N. Bozhilov, P. Maxwell, R. Nay, S.T. Heier, E. DiMasi, D. Kisailus, Materials Today 13 (2010) 42.
[36] F. Chu, D.J. Thoma, K.J. McClellan, P. Peralta, Materials Science and Engineering, A 261 (1999) 44.
[37] R.K. Wade, Journal of American Ceramic Society 75 (1992) 1682.
[38] D.G. Morris, M. Leboeuf, M.A. Morris, Materials Science and Engineering, A 251 (1998) 262.
[39] M. Patel, J. Subramanyuam, V.V.B. Prasad, Scripta Materialia 58 (2008) 211.
[40] S.C. Lim, M.F. Ashby, Acta Metallurgica 35 (1987) 1.
[41] S. Vepřek, S. Reiprich, Thin Solid Films 268 (1995) 64.
[42] S. Vepřek, Thin Solid Films 297 (1997) 145.
[43] S. Zhang, D. Sun, Y.Q. Fu, H.J. Du, Surface and Coatings Technology 198 (2005) 2.
[44] G. Mayer, Science 310 (2005) 1144.
[45] P. Fratzl, S.H. Gupta, F.D. Fischer, O. Kolednik, Advanced Materials 19 (2007) 2657.
[46] Z. Burghard, L. Zini, V. Srot, P. Bellina, P.A. Aken, J. Bill, Nano Letters 9 (2009) 4103.
[47] O. Kolednik, J. Predan, F.D. Fischer, P. Fratzl, Advanced Functional Materials 21 (2011) 3634.
[48] F. Chu, D.J. Thoma, K. McClellan, P. Peralta, Y. He, Intermetallics 7 (1999) 611.
[49] L.H. Yu, S.R. Dog, J.H. Xu, I. Kojima, Thin Solid Films 516 (2008) 1864.
[50] S. Zhang, X.L. Bui, Y. Fu, Thin Solid Films 467 (2004) 261.
[51] A. Sellinger, P.M. Weiss, A. Nguyen, Y.F. Lu, R.A. Assink, W.L. Gong, C.J. Brinker, Nature 394 (1998) 256.
[52] P.S. Tantri, E.M. Jayasingh, S.K. Biswas, S.K. Ramasesha, Materials Science and Engineering, A 336 (2002) 64.